COMPUTATIONAL INVESTIGATION AND ASSESSMENT OF NUMERICAL SCHEMES FOR ANISOTROPIC DIFFUSION EQUATIONS

Strachota, Pavel
Department of Mathematics, Faculty of Nuclear Sciences and Physical Engineering, Czech Technical University

Beneš, Michal
Department of Mathematics, Faculty of Nuclear Sciences and Physical Engineering, Czech Technical University

Grottadaurea, Marco
Department of Engineering, University of Leicester

出版情報：COE Lecture Note. 36, pp.73-83, 2012-01-27. 九州大学マス・フォア・インダストリ研究所
バージョン：
権利関係：

Proceedings of the Czech–Japanese Seminar in Applied Mathematics 2010
Czech Technical University in Prague, August 30 - September 4, 2010
pp. 73–83

COMPUTATIONAL INVESTIGATION AND ASSESSMENT OF NUMERICAL SCHEMES FOR ANISOTROPIC DIFFUSION EQUATIONS

PAVEL STRACHOTA[1], MICHAL BENEŠ[1], MARCO GROTTADAUREA[2]

Abstract. In the course of tuning the developed numerical algorithm for MR-DTI data visualization, it was necessary to introduce a measurement technique capable of quantitatively assessing the artificial isotropic diffusion in numerical schemes for PDE. Based on such assessment, a qualified choice of the numerical scheme can be made. This contribution describes the proposed measurement technique based on total variation evaluation. The procedure is applied to several numerical discretizations of the anisotropic diffusion model based on the Allen-Cahn equation and the obtained results are presented. For comparison, the traditional experimental order of convergence measurements are also provided to show their irrelevance in numerical diffusion quantification for the studied problem.

Key words. Allen-Cahn equation, artificial numerical diffusion, convergence, finite volume method, multipoint flux approximation, total variation

AMS subject classifications. 65M08, 65G99, 65D05, 35K20, 00A66

1. Introduction.

The Allen-Cahn equation having its origin in phase modeling in physics [1] has later found its application in other fields, including image processing and mathematical visualization [3, 14]. In particular, in order to visualize the streamlines of a given tensor field in 3D, an initial boundary value problem for the modified Allen-Cahn equation with incorporated anisotropy can be used [11, 14], giving similar results to the LIC method[6, 9].

The described technique for tensor field visualization is utilized in our DT-MRI tractography procedure explained in detail in [16]. However, in this contribution, the context of the medical application is omitted. Instead, focus is put on numerically solving the problem by the finite volume method using several flux approximation schemes on a rectangular grid. We also briefly comment on boundary condition treatment.

The schemes suffer from an undesired numerical dissipation effect which demonstrates itself as an additional isotropic diffusion of the solution. Hence, we proceed with the development of a measurement technique that would provide for assessing the amount of the numerical diffusion produced by the schemes. A quantitative scheme comparison criterion is thereby created. The text follows and extends the ideas briefly introduced in our recent paper [17].

2. Problem for the Allen-Cahn Equation with Anisotropy.

Formulation. Assume there is a symmetric positive definite tensor field $\boldsymbol{D} : \bar{\Omega} \mapsto \mathbb{R}^{3\times 3}$ where $\Omega \subset \mathbb{R}^3$ is a block shaped domain. On the time interval $\mathcal{J} = (0, T)$,

[1]Department of Mathematics, Faculty of Nuclear Sciences and Physical Engineering, Czech Technical University, Prague.
[2]Department of Engineering, University of Leicester

the initial boundary value problem for the anisotropic Allen-Cahn equation reads

$$\xi \frac{\partial p}{\partial t} = \xi \nabla \cdot \boldsymbol{D} \nabla p + \frac{1}{\xi} f_0(p) \qquad \text{in } \mathcal{J} \times \Omega, \tag{2.1}$$

$$\left. \frac{\partial p}{\partial n} \right|_{\partial\Omega} = 0 \qquad \text{on } \bar{\mathcal{J}} \times \partial\Omega, \tag{2.2}$$

$$p|_{t=0} = p_0 \qquad \text{in } \Omega \tag{2.3}$$

where

$$f_0(p) = p(1-p)\left(p - \frac{1}{2}\right).$$

Let $x \in \Omega$. Thanks to $\boldsymbol{D}(x)$ in the diffusion term on the right hand side of (2.1), the diffusion of p at x is focused into the direction of the principal eigenvector of $\boldsymbol{D}(x)$, or more precisely, with the directional distribution described by the ellipsoid

$$\left\{ \boldsymbol{\eta} \in \mathbb{R}^3 \middle| \, \boldsymbol{\eta}^{\mathrm{T}} \boldsymbol{D}(x)^{-1} \boldsymbol{\eta} = 1 \right\}.$$

In terms of tensor field visualization, we choose the initial condition p_0 in (2.3) as a noisy texture, in particular as a uniformly distributed impulse noise with mean value $\frac{1}{2}$. Due to the anisotropic diffusion process carried out by solving (2.1-2.3), the solution p changes in time from noise to an organized structure. Streamlines of the field of principal eigenvectors of $\boldsymbol{D}$ can be recognized there as parts with locally similar value of p. The term f_0 efficiently increases contrast of the resulting 3D image provided that the parameter ξ and the final time T are chosen appropriately (in our case by experiment). In order to actually view the resulting 3D image $p(\cdot, T)$, 2D slices through Ω can be helpful.

Numerical Solution. For numerical solution, the *method of lines* [13] is utilized. Applying a finite volume (FV) discretization scheme in space, the equation (2.1) is converted to a system of ODE in the form of a semidiscrete scheme

$$\xi \frac{\mathrm{d}}{\mathrm{d}t} p_K^h(t) = \xi \sum_{\sigma \in \mathcal{E}_K} F_{K,\sigma}(t) + \frac{1}{\xi} f_0\left(p_K^h(t)\right) \qquad \forall K \in \mathcal{T} \tag{2.4}$$

where $\mathcal{T}$ is generally an *admissible* finite volume mesh [8] with mesh size

$$h = \max_{K \in \mathcal{T}} \operatorname{diam}(K),$$

$K \in \mathcal{T}$ denotes one particular control volume (cell) and $\mathcal{E}_K$ is the set of all faces of the cell K. Thanks to the nature of the application and the geometry of Ω, $\mathcal{T}$ is chosen as a uniform rectangular mesh. $F_{K,\sigma}(t)$ represent the respective numerical fluxes at the time t, which contain difference quotients approximating the derivatives $\partial_x p$, $\partial_y p$, $\partial_z p$ at the center of the face σ. $p_K^h(t)$ is the solution of (2.4) approximating the value of $p(\boldsymbol{x}_K, t)$ where $\boldsymbol{x}_K \in K$. It is found by employing the 4th order Runge-Kutta-Merson solver with adaptive time stepping [5].

Artificial Dissipation and Finite Volume Scheme Design. As indicated in the introduction, all schemes introduce a certain amount of *artificial (numerical) isotropic diffusion* in the solution. However, its strength depends on the exact form

of $F_{K,\sigma}$. This phenomenon needs to be suppressed as much as possible as it may significantly deteriorate the visual quality of the result due to *blurring*. Its cause lies in the occurrence of high frequency structures in the solution: both the initial noise and the forming streamlines. To be treated correctly, they require the difference operators used in $F_{K,\sigma}$ to be of an appropriate order [15, 10].

We have assembled and investigated numerical schemes using the following approximations of the derivatives in the flux term:

- second order central difference approximation with linear interpolation of the missing points in the difference stencil;
- *multipoint flux approximation* (MPFA) central difference scheme with linear interpolation;
- fourth order MPFA central difference scheme with *cubic* interpolation.

Thereto, a classical forward-backward finite difference (FD) scheme has been added [15], approximating the mixed derivatives with first order only.

Details of MPFA. The MPFA schemes are used with the aim of achieving a higher order of accuracy in flux approximation. There are two forms of difference expressions used:

- The difference quotient approximating the derivative in the direction perpendicular to the face σ uses a non-equidistant point distribution in order to avoid redundant interpolation (Figure 2.1a). For simplicity, we provide here its 1-dimensional analog for a function $u \in \mathrm{C}^1(\mathbb{R})$, represented by the formula

$$\left.\frac{\mathrm{d}u}{\mathrm{d}x}\right|_{x_{i+\frac{1}{2}}} \approx \frac{1}{24h}\left(u_{i-1} - 27u_i + 27u_{i+1} - u_{i+2}\right)$$

  where $x_j = j \cdot h$, $u_j = u(x_j)$ for $j \in \mathbb{Z}, h > 0$. This formula is fourth order accurate provided that $u \in \mathrm{C}^5(\mathbb{R})$.
- The remaining derivatives are approximated using a uniform 5-point stencil. Again, its 1D analog can be written as

$$\left.\frac{\mathrm{d}u}{\mathrm{d}x}\right|_{x_i} \approx \frac{1}{12h}\left(u_{i-2} - 8u_{i-1} + 8u_{i+1} - u_{i+2}\right).$$

  Moreover, to achieve fourth order accuracy, the stencil points (Figure 2.1b) are interpolated from the neighboring grid nodes using 1-dimensional cubic interpolation. The MPFA variant using linear interpolation instead has also been investigated to verify the importance of cubic interpolation in practical cases.

Discretization of Initial and Boundary Conditions. The discrete noisy initial condition is created by randomly setting $p_K^h(0) = 0$ or $p_K^h(0) = 1$ with the same probability $\frac{1}{2}$, for each $K \in \mathcal{T}$.

The boundary condition (2.2) is implemented by extending the uniform numerical grid beyond Ω and introducing several layers of additional auxiliary grid nodes in the exterior of Ω with values of p^h mirrored along $\partial\Omega$. As a result, the numerical flux across $\partial\Omega$ evaluates to 0 thanks to central differences used in all schemes. The boundary condition is therefore approximated with the same order of accuracy as the flux itself.

Finally, it is fair to note that a slightly more suitable choice of the boundary condition could be made. The original equation (2.2) can be rewritten in the form

$$\nabla p \cdot \boldsymbol{n}|_{\partial\Omega} = 0$$

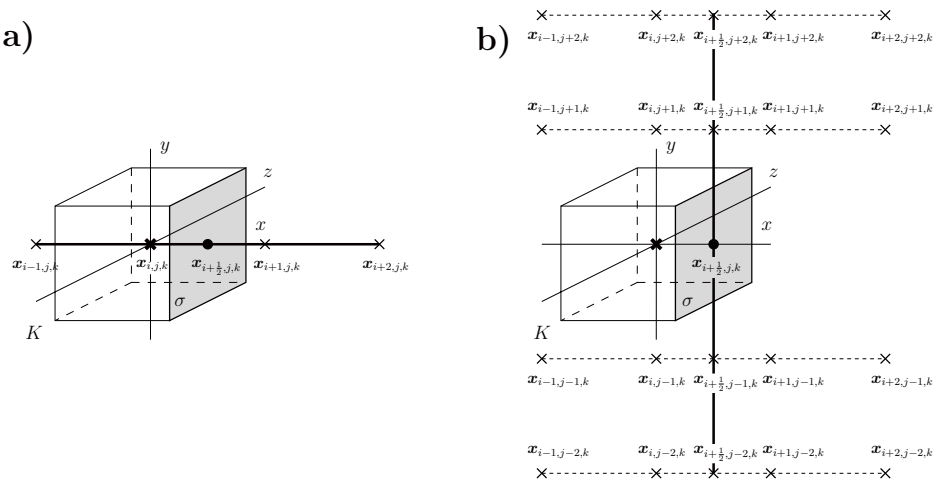

Figure 2.1: Point stencils (crosses along the thick solid lines) of difference quotients for derivative approximations in the MPFA finite volume scheme with cubic interpolation (along the dashed lines). The notation $\boldsymbol{x}_{i,j,k}$ abbreviates $\boldsymbol{x}_{K_{i,j,k}}$ where the indices i, j, k are used to identify the cells $K_{i,j,k}$ of a uniform rectangular mesh.

and replaced by

$$(D\nabla p) \cdot \boldsymbol{n}|_{\partial\Omega} = 0, \tag{2.5}$$

as e.g. in [7]. However, the auxiliary node approach cannot be used easily in this case. Instead, (2.5) can be treated explicitly by adjusting the numerical scheme accordingly close to the boundary. Due to implementation complexity, the boundary condition of this form has been avoided so far.

3. Artificial Diffusion Measurement. Having the results available obtained by using different schemes but based on identical input settings, one can try to compare them visually to decide on the scheme with the least artificial diffusion. In Figure 3.1, an example of such comparison is demonstrated on a real-data DT-MRI neural tract visualization. In the center part of the images, a major neural tract in the shape of U is displayed in the form of streamlines. It can be observed that the FD scheme produces undesired isotropic diffusion greatly dependent on the prescribed direction of diffusion. This is related to the asymmetry of the difference stencil. The 2nd order central difference flux approximation used in the FV scheme is already symmetric. However, it is clearly outperformed by the scheme based on MPFA which causes significantly weaker blurring.

Scheme Assessment by Total Variation. In this part we introduce a quantitative measure of the artificial diffusion in the schemes. For this purpose, the total variation of the numerical solution $p^h = p^h(t)$ finds its rather unusual application. It is defined as

$$TV\left(p^h\right) = \sum_{K \in \mathcal{T}} \left|\nabla_h p_K^h\right| m(K) \tag{3.1}$$

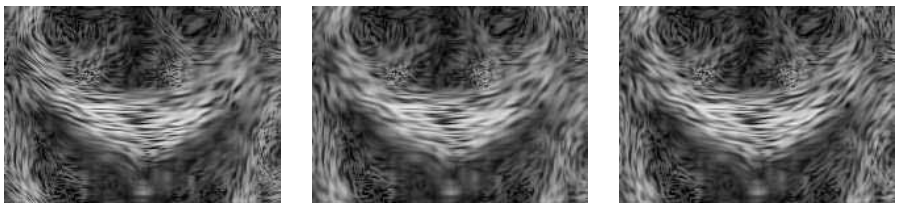

FD FV 2nd order MPFA cubic 4th order

Figure 3.1: Artificial diffusion in different numerical schemes. Crops from colorized MR-DTI visualizations based on real data, transverse plane slice.

where $\nabla_h p_K^h$ represents the discrete approximation of the gradient and $m(K)$ is the measure of the cell K. From the image processing point of view, the value of TV is proportional to both the number of edges in the image p^h and its contrast. Both these quantities assume their maxima for the noisy initial condition and change in time along with the diffuse evolution of the numerical solution. Performing two computations with identical settings except for the choice of the numerical scheme, it is possible to directly compare the TV values of the results. The scheme producing an image with a greater value of TV exhibits less artificial diffusion as it maintains more edges, more contrast, or both.

Scheme Comparison Methodology. We have performed extensive testing with phantom input tensor fields to investigate the behavior of the schemes depending on the prescribed direction of diffusion. For each triple of spherical coordinates $(r = 1, \varphi, \theta)$ where $\varphi \in [0, 360°]$, $\theta \in [-90°, 90°]$, let a unit vector

$$\boldsymbol{v}_1(\varphi, \theta) = (\cos\varphi\cos\theta, \sin\varphi\cos\theta, \sin\theta)$$

represent the principal eigenvector of a uniform tensor field $\boldsymbol{D}(\varphi, \theta)$, corresponding to the eigenvalue $\lambda_1 = 100$. The remaining eigenvalues are $\lambda_2 = \lambda_3 = 1$ and the eigenvectors $\boldsymbol{v}_2, \boldsymbol{v}_3$ complete the orthonormal basis of R^3. Afterwards, a computation is carried out using $\boldsymbol{D}(\varphi, \theta)$ as input data.

Subsequently, TV is evaluated from the resulting datasets. The TV values alone are not of particular interest since they depend on both the grid dimensions and the size of the domain Ω. However, the relative differences of TV between schemes provide the desired information.

The results of the procedure described above performed for all the four schemes in several time levels are shown in Figures 3.2-3.6. In each chart, TV is normalized so that its maximum over all plotted data series is 1. Settings of all important computation parameters can be found in the figure captions. The initial condition $p_K^h(0)$ is random for each computation, although theoretically it should stay fixed for all φ, θ to keep the comparison absolutely correct. Nevertheless, it turns out that repeated computations with the same setting and random $p_K^h(0)$ result in negligible differences ($< 1\%$) in the value of TV. This also proves the robustness of this method with respect to the choice of the initial condition as long as its statistical properties are maintained.

In Figure 3.2, the latitude θ is fixed to 0 and the longitude φ traverses the angles from 0° to 350° with the step 10°. The same is true for Figure 3.3 which only differs from Figure 3.2 in the setting of parameter ξ. Figure 3.4 depicts the "diagonal" cut

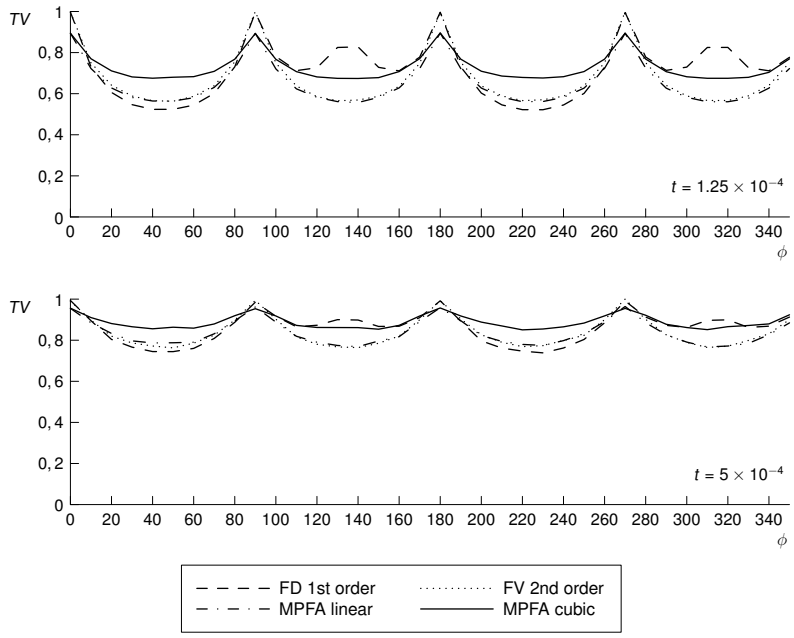

Figure 3.2: Comparison of numerical schemes based on TV, $\xi = 5 \times 10^{-3}$, $\theta = 0$, $\varphi \in [0°, 350°]$.

through the space (φ, θ) in the range from 0° to 90°, including the worst situation for all schemes where $\varphi = \theta = 45°$. Finally, Figures 3.5 and 3.6 contain surface plots of all measured combinations of φ, θ for the FD scheme and the MPFA FV scheme with cubic interpolation, respectively. For all computations, a uniform grid of $200 \times 200 \times 200$ cells was used.

Observations from Figures 3.2-3.6 can be summed up as follows:

- Artificial diffusion clearly depends on $\boldsymbol{v}_1$ and occurs least when the direction $\boldsymbol{v}_1$ is aligned with coordinate axes. For the FD scheme, a straightforward explanation can be given: In the degenerate case $\lambda_2 = \lambda_3 \to 0$, the equation systems for different rows of grid nodes along $\boldsymbol{v}_1$ become independent.
- The performance of all schemes improves (i.e. TV rises) with growing time. This is obvious as the ongoing diffusion gradually limits the frequency spectrum of the solution. At the beginning, the infinite spectrum of the initial condition can not be handled properly by any difference operator.
- The performance of the schemes improves with decreasing ξ (compare Figures 3.2 and 3.3).
- The FD scheme exhibits a highly asymmetric behavior, whereas all FV schemes are symmetric (see Figures 3.3 and 3.5 and compare visually to Figure 3.1).
- The FV scheme with MPFA and cubic interpolation outperforms all other schemes in the comparison except for the FD scheme when $\boldsymbol{v}_1$ is aligned with some coordinate axis.

Extension to Real DT-MRI Data Visualization. One may ask whether the described technique can serve as an efficient tool of numerical diffusion measurement in the case of real (and complicated) input tensor data. At the first sight, such

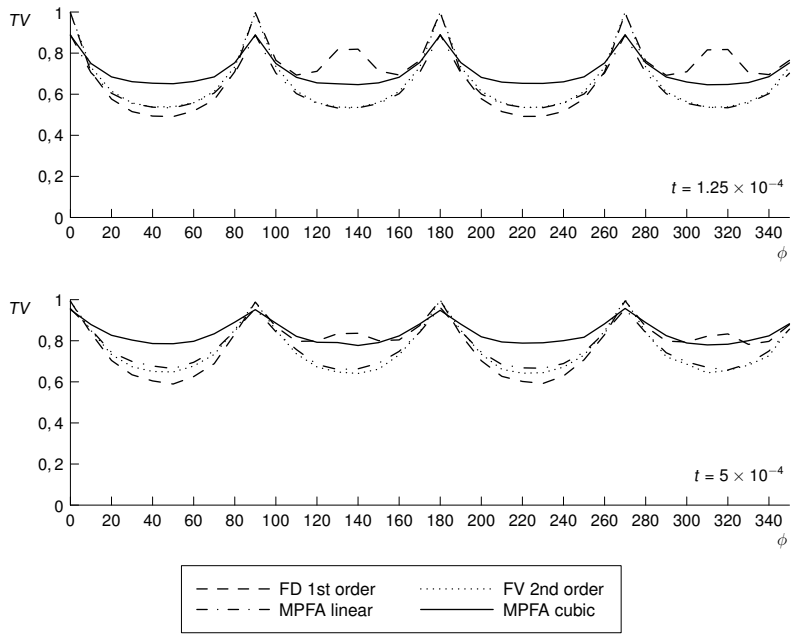

Figure 3.3: Comparison of numerical schemes based on TV, $\xi = 10^{-2}$, $\theta = 0$, $\varphi \in [0°, 350°]$.

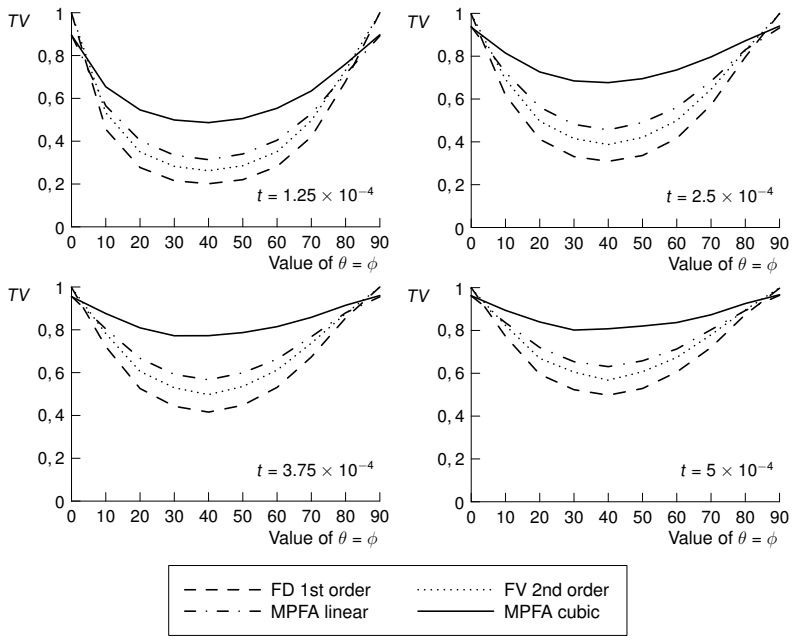

Figure 3.4: Comparison of numerical schemes based on TV in different time levels, $\xi = 10^{-2}$, $\theta \in [0°, 90°]$, $\varphi = \theta$.

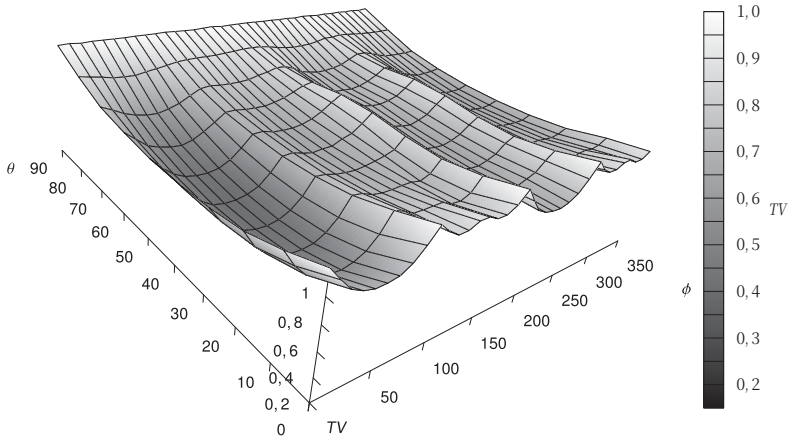

Figure 3.5: TV graph for the FD scheme, $t = 3.75 \times 10^{-4}$, $\xi = 5 \times 10^{-3}$, $\theta \in [0°, 90°]$, $\varphi \in [0°, 350°]$.

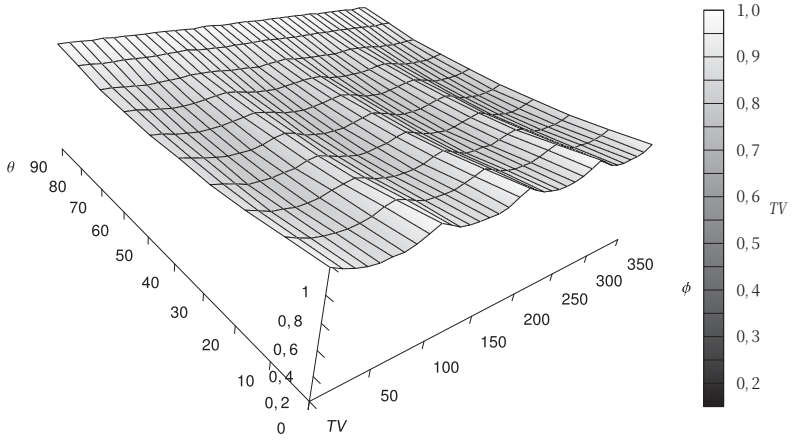

Figure 3.6: TV graph for the FV scheme with MPFA and cubic interpolation, $t = 3.75 \times 10^{-4}$, $\xi = 5 \times 10^{-3}$, $\theta \in [0°, 90°]$, $\varphi \in [0°, 350°]$.

a measurement might be considered more relevant with respect to the purpose of the solved problem. However, TV is an integral quantity and as such it averages the numerical diffusion over the domain Ω. From the results above, it follows that significant differences in numerical schemes appear for some directions of anisotropy only. Regions where the diffusion is steered to these directions may be small compared to the volume of Ω. As a consequence, TV measurement will not testify to a clear distinction between performances of any two numerical schemes although the local differences in the numerical solution may be crucial.

Let us also briefly mention another problem, which luckily has quite a simple solution for DT-MRI data visualization. The numerical diffusion gets stronger together with the anisotropy strength. It is therefore useful to restrict the evaluation of TV in (3.1) to such areas where the diffusion is anisotropic enough. The quantity expressing

h	$L_\infty(\mathcal{J};L_2(\Omega))$ error $\times 10^{-4}$	EOC in $L_\infty(\mathcal{J};L_2(\Omega))$	$L_\infty(\mathcal{J};L_\infty(\Omega))$ error $\times 10^{-2}$	EOC in $L_\infty(\mathcal{J};L_\infty(\Omega))$
0.00990	4.4982	-	1.0613	-
0.00497	1.1830	1.940	0.2957	1.857
0.00332	0.5328	1.975	0.1352	1.938
0.00249	0.3013	1.987	0.0769	1.966

Table 3.1: EOC results for the FV scheme with 2nd order flux approximation, anisotropic case, Dirichlet b.c.

the anisotropy strength and called *fractional anisotropy* (FA) can be calculated from the eigenvalues of $\boldsymbol{D}(\boldsymbol{x})$. It is used in MRI for several purposes [2, 4]. Evaluating TV only in the regions where $FA >$ given_threshold fulfills the above requirement and also excludes the regions outside the brain where no diffusion occurs and the initial noise remains intact. For the input data used in Figure 3.1, the experiments indicate TV improvement in the order of tens of percent in favor of the MPFA scheme with cubic interpolation compared to the rest of the schemes.

Experimental Order of Convergence. Evaluation of the experimental order of convergence (EOC) is a routine tool for numerical scheme verification [12]. The solution is computed on a sequence of gradually refining grids, making it possible to calculate the ratio

$$\mathrm{EOC}_i = \log\left(\frac{\mathrm{Error}_i}{\mathrm{Error}_{i-1}}\right) \Big/ \log\left(\frac{h_i}{h_{i-1}}\right)$$

where $h = \max_K \operatorname{diam}(K)$ is the mesh size and Error_i is the difference of the i-th solution from the precise (analytical) solution measured in an appropriate norm. To be able to calculate the analytical solution, the right hand side of (2.1) is modified to obtain an alternate problem with any prescribed solution of class $C^2\left(\bar{\Omega}\times\mathcal{J}\right)$. In contrast to TV evaluation, smooth enough solutions are necessary for the EOC measurement to make sense. Of course, the prescribed solution must satisfy the initial and boundary condition.

Measurements were performed for all schemes introduced in Section 2 with both Dirichlet and homogeneous Neumann boundary conditions. In addition, isotropic and anisotropic constant tensor fields were taken into account. It has been found that all schemes in all measurement variants exhibit EOC ≈ 2. This result confirms the conclusion that EOC and TV measurements produce unrelated results, rendering the EOC incapable of capturing artificial diffusion behavior in the numerical schemes.

A more detailed examination reveals, though, that the MPFA schemes produce a smaller absolute error on the same grid size compared to the scheme based on the standard 2nd order flux approximation (see Table 3.1 and 3.2). This observation is in agreement with the expected behavior. However, it still gives little information about artificial diffusion.

4. Conclusion. We have developed an approach for measuring the amount of artificial isotropic diffusion in numerical schemes. Thorough computational studies based on phantom input data confirm that this technique fulfills the given objective and produces results in agreement with an intuitive notion of blurring observable

h	$L_\infty(\mathcal{J};L_2(\Omega))$ error $\times 10^{-4}$	EOC in $L_\infty(\mathcal{J};L_2(\Omega))$	$L_\infty(\mathcal{J};L_\infty(\Omega))$ error $\times 10^{-3}$	EOC in $L_\infty(\mathcal{J};L_\infty(\Omega))$
0.00971	1.3357	-	3.0835	-
0.00493	0.3395	2.019	0.8407	1.915
0.00330	0.1522	2.002	0.3840	1.956
0.00248	0.0860	2.000	0.2189	1.970

Table 3.2: EOC results for the FV scheme with MPFA and cubic interpolation, anisotropic case, Dirichlet b.c.

in images obtained by solving (2.4). Introducing a suitable threshold in (3.1), the measurement can also be applied to computations with real DT-MRI input data.

The results provide the necessary information for a qualified choice of the numerical scheme for solving anisotropic diffusion problems. The evaluation of EOC can only serve as an ancillary tool in numerical diffusion assessment.

Acknowledgments: This work was carried out under the HPC-EUROPA++ project (project number: 211437), with the support of the European Community - Research Infrastructure Action of the FP7 "Coordination and support action" Program. This work was supported by the Grant Agency of the Czech Technical University in Prague, grant No. SGS10/086/OHK4/1T/14. Support of the project of the Ministry of Education of the Czech Republic MSM6840770010 "Applied Mathematics in Technical and Physical Sciences". Partial support of the project "Jindřich Nečas Center for Mathematical Modeling", No. LC06052. Special thanks to the colleagues at the Institute for Clinical and Experimental Medicine (IKEM) in Prague for providing input datasets, consultations, and support.

REFERENCES

[1] S. Allen and J. W. Cahn, *A microscopic theory for antiphase boundary motion and its application to antiphase domain coarsening*, Acta Metall. **27** (1979), 1084–1095.

[2] P. J. Basser and C. Pierpaoli, *Microstructural and physiological features of tissues elucidated by quantitative-diffusion-tensor MRI*, J. Magn. Reson. **111** (1996), 209–219.

[3] M. Beneš, V. Chalupecký, and K. Mikula, *Geometrical image segmentation by the Allen-Cahn equation*, Appl. Numer. Math. **51** (2004), 187–205.

[4] D. L. Bihan et al., *Diffusion tensor imaging: Concepts and applications*, J. Magn. Reson. Imaging. **13** (2001), 534–546.

[5] J. C. Butcher, *Numerical Methods for Ordinary Differential Equations*, Wiley, 2003.

[6] B. Cabral and L. C. Leedom, *Imaging vector fields using line integral convolution*, in SIGGRAPH '93: Proceedings of the 20th annual conference on Computer graphics and interactive techniques, New York, NY, USA, 1993, ACM, pp. 263–270.

[7] O. Drblíková, A. Handlovičová, and K. Mikula, *Error estimates of the finite volume scheme for the nonlinear tensor-driven anisotropic diffusion*, Appl. Numer. Math. **59** (2009), 2548–2570.

[8] R. Eymard, T. Gallouët, and R. Herbin, *Finite volume methods*, in Handbook of Numerical Analysis, P. G. Ciarlet and J. L. Lions, eds., vol. 7, Elsevier, 2000, pp. 715–1022.

[9] E. Hsu, *Generalized line integral convolution rendering of diffusion tensor fields*, in Proc. Intl. Soc. Mag. Reson. Med **9** (2001), 790.

[10] H. Lomax, T. H. Pulliam, and D. W. Zingg, *Fundamentals of Computational Fluid Dynamics*, Springer, 2001.

[11] T. Preusser and M. Rumpf, *Anisotropic nonlinear diffusion in flow visualization*, in Proceedings of IEEE Visualization 1999, 1999, pp. 325–332.

[12] J. R. Rice and M. Mu, *An experimental performance analysis for the rate of convergence of 5-point star on general domains*, tech. rep., Department of Computer Sciences, Purdue University, 1988.

[13] W. E. Schiesser, *The Numerical Method of Lines: Integration of Partial Differential Equations*, Academic Press, San Diego, 1991.

[14] P. Strachota, *Vector field visualization by means of anisotropic diffusion*, in Proceedings of Czech Japanese Seminar in Applied Mathematics 2006, M. Beneš, M. Kimura, and T. Nakaki, eds., vol. 6 of COE Lecture Note, Faculty of Mathematics, Kyushu University Fukuoka, 2007, pp. 193–205.

[15] ———, *Antidissipative numerical schemes for the anisotropic diffusion operator in problems for the Allen-Cahn equation*, in ALGORITMY 2009 - Proceedings of contributed lectures and posters, A. Handlovičová, P. Frolkovič, K. Mikula, and D. Ševčovič, eds., vol. 18, Slovak University of Technology in Bratislava, 2009, pp. 134–142.

[16] ———, *Implementation of the MR tractography visualization kit based on the anisotropic Allen-Cahn equation*, Kybernetika **45** (2009), 657–669.

[17] P. Strachota and M. Beneš, *A multipoint flux approximation finite volume scheme for solving anisotropic reaction-diffusion systems in 3D*, in Finite Volumes for Complex Applications VI - Problems & Perspectives, J. Fořt, J. Fürst, J. Halama, R. Herbin, and F. Hubert, eds., Springer, 2011, pp. 741–749.